applied sciences

MDPI

Article

Investigation of Annealing Process Effects on the Response and Stability of Sprayed Co_2SnO_4 Film under Ethanol Vapor

Ahmed Labidi [1,2]

[1] Department of Physics, College of Science and Arts at Ar-Rass, Qassim University, Buraydah 51921, Saudi Arabia; l.ahmed@qu.edu.sa; Tel.: +966-532414278
[2] Laboratory of Materials Molecules and Applications (LMMA), IPEST, Carthage University, La Marsa 2070, Tunisia

Abstract: The ethanol (C_2H_5OH) vapor detection properties of a layer of cubic spinel cobalt stannate as-prepared Co_2SnO_4 (denoted as CTO_{as}), elaborated by a low-cost spray pyrolysis method, were investigated before and after an annealing process. The response of layers under ethanol vapors of different concentrations exhibited a stable behavior in a dry atmosphere at the optimum working temperatures. The elaborated nanomaterials were characterized by transmission electron microscopy (TEM), scanning electron microscopy (SEM), X-ray diffraction (XRD), direct current measurement (DC) and impedance spectroscopy techniques (AC). After the annealing process of pure CTO_{as}, an n-type to p-type conductivity switch was observed and attributed to Co_3O_4 apparition in the Co_2SnO_4 structure. The layer's ethanol response increased and became more stable after annealing. The stability was measured over a period of three months. DC and AC investigations allowed us to propose a detection mechanism involving grain boundary regions in a Co_2SnO_4/Co_3O_4 composite obtained after annealing (denoted as CTO_{ann}). According to its stable and receivable sensing response, the Co_2SnO_4/Co_3O_4 composite could be considered as a promising novel sensitive layer for ethanol gas sensors.

Keywords: Co_2SnO_4; Co_2SnO_4/Co_3O_4 composite; grain boundary; ethanol; spray pyrolysis; gas sensor; interaction mechanism

Citation: Labidi, A. Investigation of Annealing Process Effects on the Response and Stability of Sprayed Co_2SnO_4 Film under Ethanol Vapor. *Appl. Sci.* **2023**, *13*, 2797. https://doi.org/10.3390/app13052797

Academic Editor: Sang Sub Kim

Received: 3 January 2023
Revised: 7 February 2023
Accepted: 13 February 2023
Published: 22 February 2023

1. Introduction

Currently, the pollution crisis is one of the major global problems. In order to overcome this problem, several research groups have turned their attention towards various kinds of nanomaterials, because such materials exhibit outstanding performance in gas sensor applications for controlling the emission of polluting gases. A ternary metal oxide and composites such as $NiMn_2O_4$, Fe_2O_3/ZnO and Ag-$SnO_2/\beta C_3N_4$ [1–3] have been developed as promising materials for use in gas sensing applications. Other materials, such as metal stannates including Ba_2SnO_4, Ca_2SnO_4, Zn_2SnO_4, Cd_2SnO_4, Mg_2SnO_4, Mn_2SnO_4 and Co_2SnO_4, have also been developed by research groups [4–10]. These materials have been found to have interesting properties and demonstrated good optical and electrical performance, and have been widely used in the study of solar cells, super capacitors, etc. [11–18]. So far, there have been very few studies on their gas sensing performance.

In this context, special attention has been paid to the cobalt stannate Co_2SnO_4 (CTO), which has the potential for many applications in various fields, including thermally stable capacitors [19]. Nevertheless, little study has been undertaken in the field of Co_2SnO_4 synthesis, or on its gas detection properties. Thus, to the best of our knowledge, synthesis of Co_2SnO_4 by the technique of spray pyrolysis and the study of its sensing properties under ethanol vapor (EtOH) has not been yet reported. In addition, there has been no study of the sensing properties of Co_2SnO_4/Co_3O_4 composite under ethanol vapor. Among the most commonly used materials for ethanol detection are Co_3O_4 [20–22] and its composites, such

as ZnO/Co_3O_4, $Fe_2O_3@Co_3O_4$, $Co_3O_4–TiO_2$ and $Co_3O_4/Ti_3C_2T_x$ [23–26]. Most sensing devices for various kinds of gases are based on metallic oxide layers [27]. In the present work, the low-cost technique of spray pyrolysis followed by an annealing process was successfully used to synthetize ternary Co_2SnO_4 and also Co_2SnO_4/Co_3O_4 sensing layers for ethanol (EtOH) vapor detection. The Co_2SnO_4/Co_3O_4 composite was the resultant product from an annealing treatment, as we will show later in this work.

Ethanol vapor was chosen as the target gas in this study, due to its toxicity [28] and its application in other safety sectors. Thus, there is a necessity to develop more effective sensors for ethanol detection [29]. Therefore, many ethanol sensing methods based on physical and chemical processes have been developed [30]. In all these methods, different materials were tested in order to find an appropriate material with the best sensitivity and selectivity under ethanol vapor to be used as the active layer for an ethanol gas sensor in a given application. Such sensors could be used, for example, in food quality checks, or in the bioenergy industry in ethanol production. Ethanol is also considered as a renewable fuel, which can be produced from various materials and plants, collectively known as "biomass". In this context, Co_2SnO_4 could be introduced as a promising new candidate for the ethanol gas sensor industries. The morphological characterizations of our prepared Co_2SnO_4 film, as well as its ethanol sensing properties and sensing mechanism, were investigated according to the annealing temperature.

2. Experimental Procedure

2.1. Co_2SnO_4 Film Deposition

Co_2SnO_4 (CTO) films were obtained using 0.02 mole of cobalt (II) chloride dihexahydrate ($CoCl_2.6H_2O$) mixed with 0.01 M of chloride dihydrate ($SnCl_2.2H_2O$) in 100 mL of distilled water at ambient temperature. All the used reagents were commercially available, and no purification was needed. Then, 2.0 M of NaOH solution, used as mineralizer, was added under magnetic stirring for 15 min; a blue precipitate was obtained instantaneously. The final molar ratio of [Sn]:[Co] was fixed at 1:2. The mixture was then transferred to Teflon-lined stainless steel autoclave and kept at 240 °C for 48 h. The resulting precipitates were collected by centrifugation and washed with distilled water, and finally dried in an electric oven at 120 °C for 12 h. The obtained Co_2SnO_4 precursor was dissolved in absolute alcohol and sprayed on glass substrates at a growth temperature of 500 °C.

During the spray deposition, nitrogen (N_2) was used as a carrier gas. In addition, to ensure the best uniformity of the deposited layers, the horizontal sweep of the nozzle (0.5 mm diameter) was optimized. The flow rate of the precursor mixture was taken constantly at 5 $mL.min^{-1}$. After deposition, the elaborated films were allowed to cool to room temperature.

Finally, two Co_2SnO_4 samples were prepared. One of them (denoted as CTO_{ann}) was calcined at 800 °C for 8 h with a heating rate of 10 °C/min under standard atmospheric conditions, after which the sample was allowed to cool to room temperature. The aim of this step was the investigation of the annealing effects on the Co_2SnO_4 layer's sensitivity toward ethanol vapor, which is probably controlled by the phase transition in the as-prepared layer. The choice of temperature and calcination duration were in order to ensure the synthesis of a stable sensitive phase, as the working temperatures under the ethanol vapor would be varied. The second sample, which remained as prepared, was denoted as CTO_{as}. The morphological results are reported in Figure 1.

We noted that the surface morphologies of CTO_{ann} (Figure 1b) were more granular and porous compared with the as-prepared sample (CTO_{as}) presented in Figure 1a. These morphological differences could be beneficial for ethanol detection by CTO_{ann}.

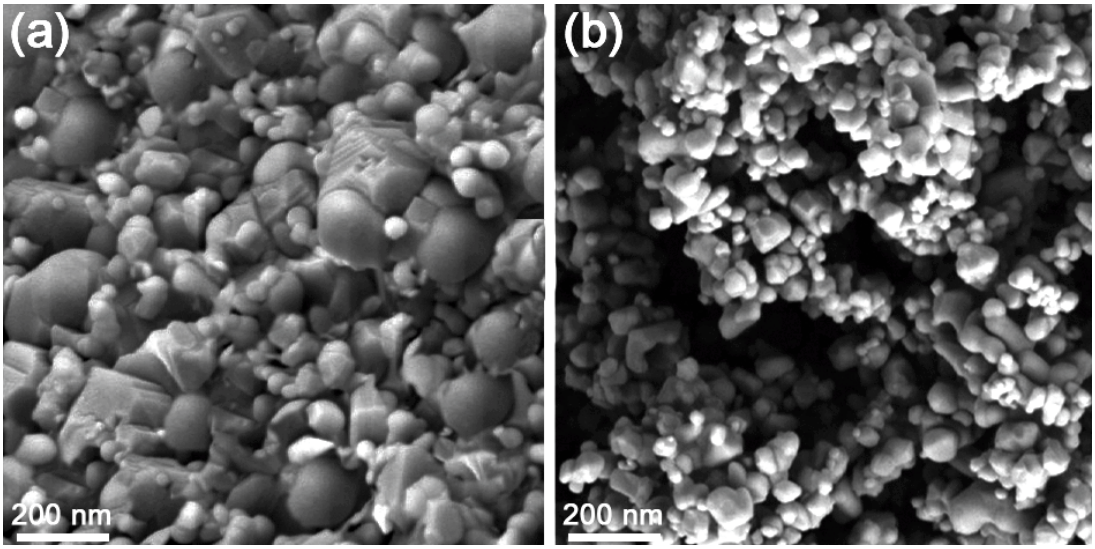

Figure 1. SEM images: (**a**) as-prepared sample CTO_{as}; (**b**) annealed sample CTO_{ann}.

2.2. Characterization Techniques

The layers' X-ray diffraction (XRD) characterizations were performed using a Philips X'Pert MPD XRD diffractometer with monochromatic radiation Cu-Kα (1.51418 Å), in the range of 20–80°, with a scanning rate of $0.05°.s^{-1}$. SEM investigations were undertaken using a JSM-6510 scanning electron microscope from JEOL, Ltd., with accelerating voltage (0.5 kV to 30.0 kV) at low vacuum (10 Pa–150 Pa) and magnification up to 600,000×. The prepared samples were also characterized by a Tecnai F20 (200 kV) transmission electron microscope (TEM) from FEI. The samples' DC and AC gas sensor electrical signals were measured using a source/pico-ammeter HP4140B and Solartron 1250 impedance analyzer from L.M.M.A laboratory, respectively, at a low-bias voltage of 50 mV.

2.3. Experimental Setup for Ethanol Detection

Figure 2 presents the experimental setup used for ethanol detection in which the sensors were exposed to a flow rate of 1 $L.min^{-1}$ of dry air used as a carrier gas for ethanol vapor coming from a flask placed in a heating bath. The ethanol concentrations were controlled by two mass flows (d_1, d_2) and given by the following equation [31].

$$[C_{EtOH}](ppm) = \left(\frac{xd_1}{(1+x)d_1 + d_2}\right) \times 10^6 \quad (1)$$

The vapor molar fraction x at fixed T_{vap} was given by:

$$x = \frac{P_{vap}}{P_{atm}} \quad (2)$$

P_{atm} and P_{vap} were the atmospheric and partial vapor pressure, respectively, in the test chamber [32]. For all ethanol concentrations, the heated bath circulator temperature T_{vap} was fixed at 30 °C in order to fix the vapor pressure P_{vap} which was deduced from the database curve of ethanol pressure from the *CRC Handbook of Chemistry and Physics* [33].

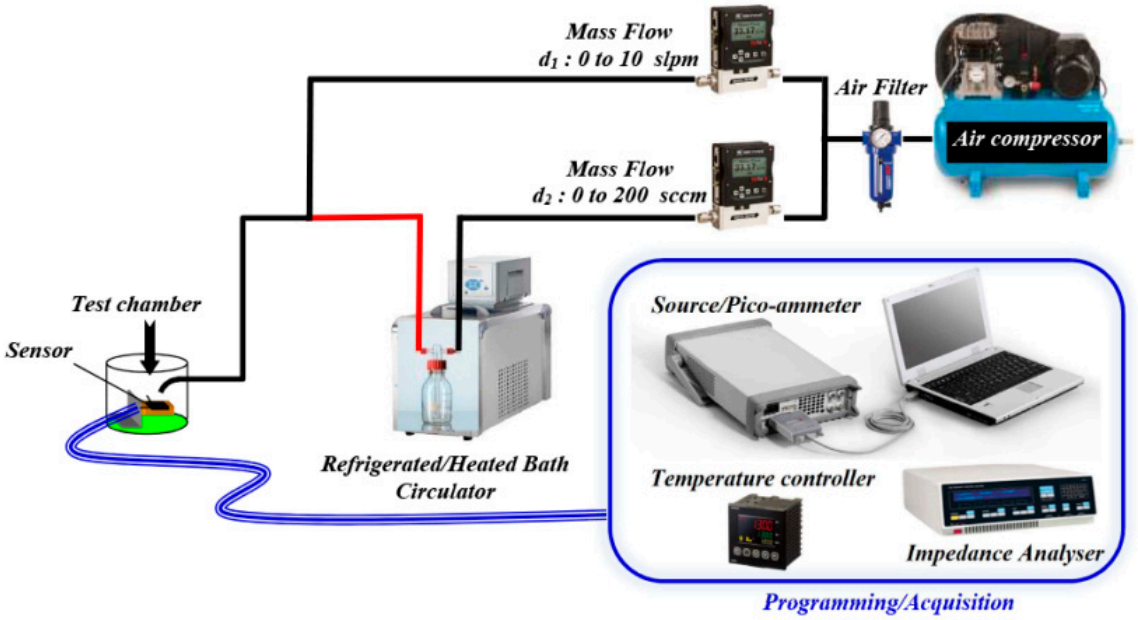

Figure 2. Gas sensing setup.

3. Results and Discussion

3.1. Characterization of Elaborated Films

The XRD layer pattern of the as-prepared sample (CTO_{as}) confirmed the synthesis of pure Co_2SnO_4 with a spinel phase, as shown in Figure 3. All diffraction peaks could be indexed in the JCPDS 29-0514 card for the Co_2SnO_4 spinel cubic single phase. After annealing, the obtained sample (CTO_{ann}) was identified as a mixture of spinel Co_2SnO_4 phase and spinel Co_3O_4 pure phases; the obtained Co_2SnO_4/Co_3O_4 composite was indexed by both standard cards: JCPDS no. 29-0514 for the Co_2SnO_4 spinel phase and JCPDS 78-1970 for the Co_3O_4 spinel phase.

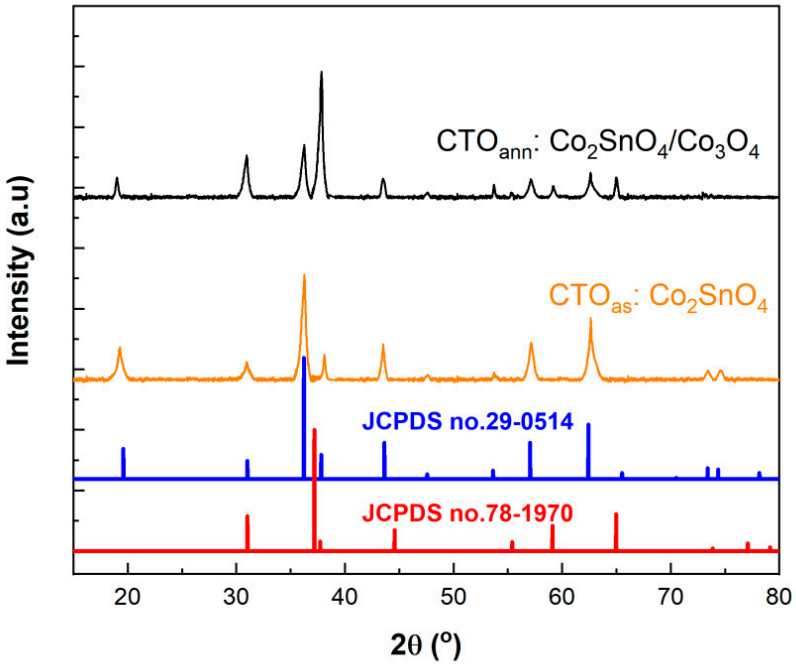

Figure 3. XRD pattern of the as-prepared (CTO_{as}) and annealed (CTO_{ann}) Co_2SnO_4 films.

The crystallite sizes of the prepared samples were calculated using the following Scherrer formula (Equation (3)):

$$D_{hkl} = \frac{0.9\,\lambda}{\beta.\mathrm{Cos}\theta} \quad (3)$$

where λ is the wavelength of the implemented X-ray diffraction, β is the full width at half maximum (FWHM) of the (hkl) diffraction plane in radians and h is the corresponding incident angle.

The average crystallite sizes were found to be about 80 nm for the CTO_{as} pure Co_2SnO_4 (311) phase and 50 nm and 30 nm for the Co_2SnO_4 (311) and Co_3O_4 (111) directions, respectively. In the polycrystalline CTO_{ann} layer, no other phase formation of impurities was observed in the diffractogram. Figure 4a,b show the high-magnification SEM images of the samples obtained before and after the annealing treatment at 800 °C.

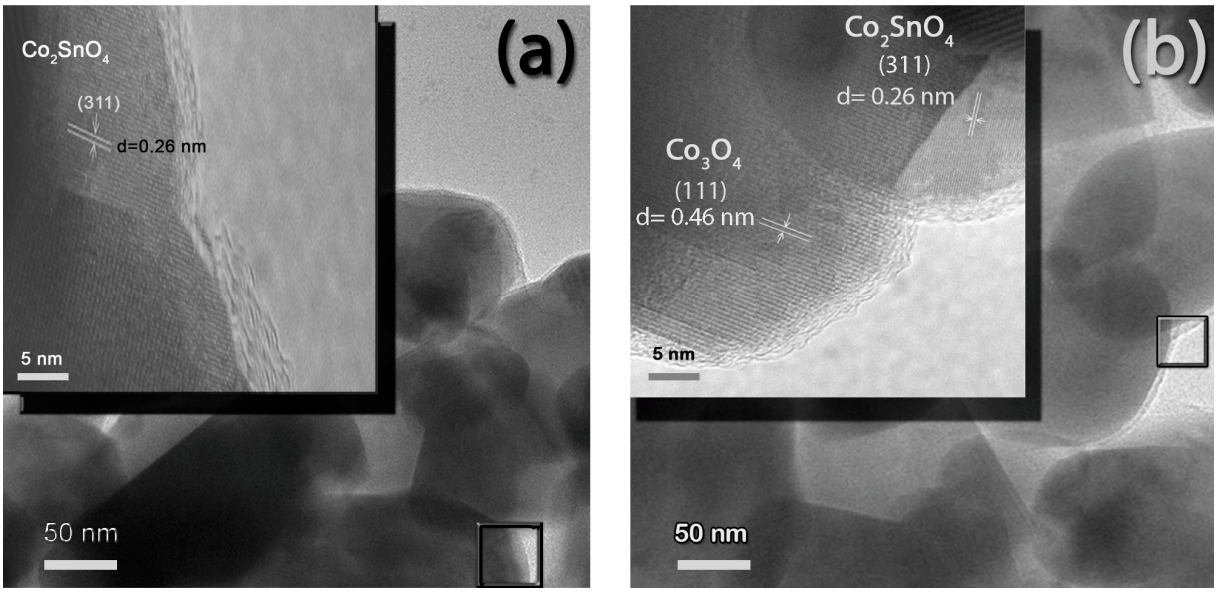

Figure 4. TEM images of pure Co_2SnO_4 (**a**) and Co_2SnO_4/Co_3O_4 composite (**b**).

We note that the high-magnification SEM image shows a random combination of compact grain agglomerations with average sizes ranging from about 50 nm to 150 nm in size. After annealing, the film shows a large number of individual grains with average sizes ranging from about 20 nm to 50 nm in size, leading to an increase in porosity and offering a large active surface area available for oxygen molecule adsorption.

High surface area is the main factor in a sensor's sensitive layer which enables it to achieve higher sensitivity.

The polycrystalline nature of the annealed film offered a greater available surface area for atom fraction and oxygen molecule adsorption on the surfaces of grains and at interfaces between grains (grain boundaries), suggesting that the microstructure of the films is suitable for ethanol vapor sensing applications. The variations in the sizes of particles seen in SEM images were comparable to the grain sizes estimated by XRD measurements.

In addition, the phase transition from Co_2SnO_4 (CTO_{as}) to Co_2SnO_4/Co_3O_4 composite (CTO_{ann}) was confirmed by TEM images (Figure 4). Figure 4a shows the Co_2SnO_4 (311) monocrystal structure of the as-prepared film with an interplanar spacing of 0.26 nm, whereas Figure 4b shows the multicrystal structure of the annealed film with high crystallinity and purity. The interplanar spacing for CTO_{as} and CTO_{ann} is calculated as 0.26 nm and 0.46 nm, respectively, matching well with the interplanar spacing of Co_2SnO_4 (311) and Co_3O_4 (111), and confirming the elaboration of the Co_2SnO_4/Co_3O_4 composite.

3.2. Co_2SnO_4 and Co_2SnO_4/Co_3O_4 Sensing Results and Discussion under Ethanol

The samples' ethanol sensing tests were performed in the concentration range of ethanol vapor at 100–1000 ppm; the gas response "S" is defined as follows:

$$S = \frac{I_{gas} - I_0}{I_0} \quad (4)$$

for the CTO_{as} sample, which presented the conductivity behavior of an n-type semiconductor; and

$$S = \frac{I_{gas} - I_0}{I_{gas}} \quad (5)$$

for the CTO_{ann} sample, which showed the conductivity behavior of a p-type semiconductor.

I_{gas} and I_0 are the current intensities of layers under ethanol gas (vapor) and dry air, respectively. Firstly, in order to determine the optimal working temperatures, the concentration of ethanol was fixed at 500 ppm and the temperature was varied from 100 °C to 250 °C. The obtained optimal working temperatures were found to be 150 °C for CTO_{as} and 200 °C for CTO_{ann}, as shown in Figure 5a,b.

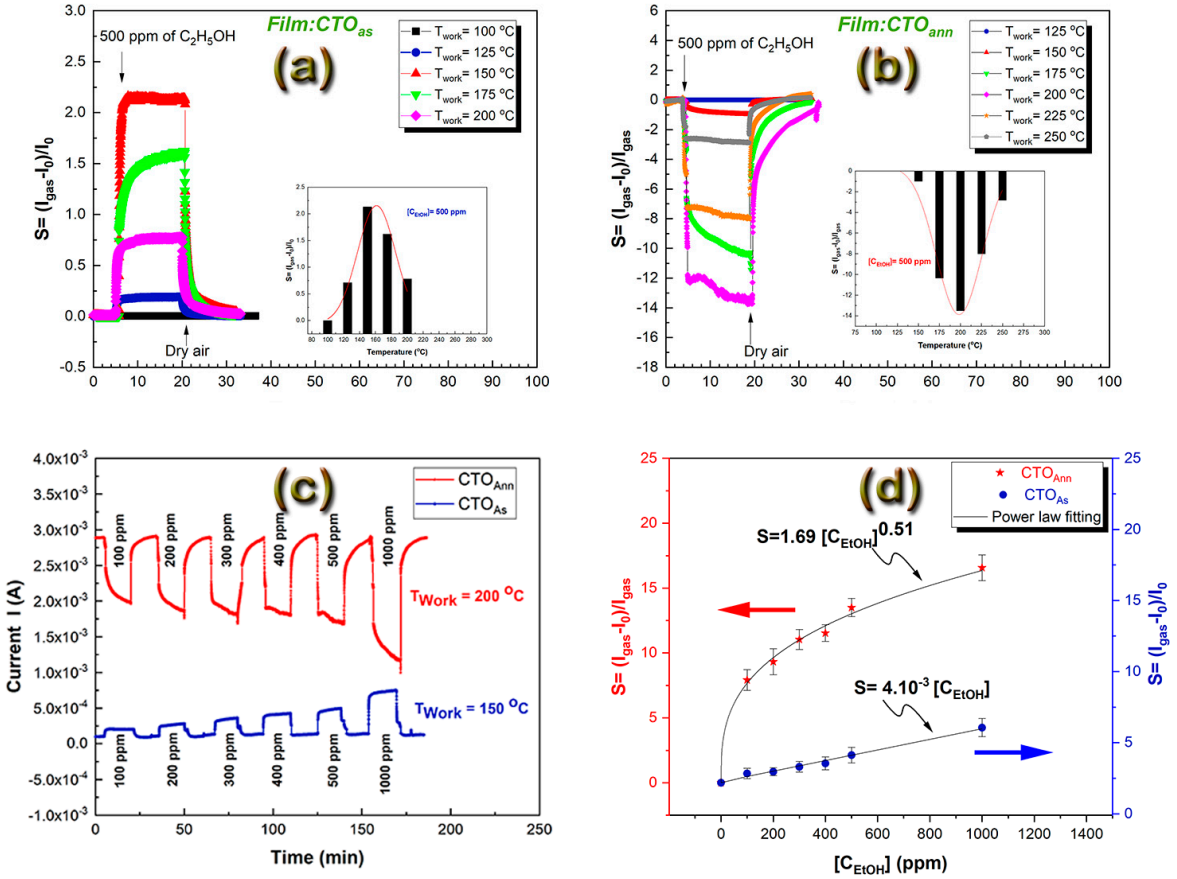

Figure 5. CTO_{as} and CTO_{ann} ethanol sensing results: (**a**) optimal working temperature determination of as-prepared film (CTO_{As}) under 500 ppm of ethanol; (**b**) optimal working temperature determination of annealed film (CTO_{Ann}) under 500 ppm of ethanol; (**c**) dynamic current variation of prepared layers at optimum temperatures; (**d**) layers' response evolutions versus ethanol concentration.

After optimal working temperature deduction, a dynamic measurement under gas was made in order to deduce the response (τ_{res}) and the recovery (τ_{rec}) times, reported in the last table. The chemical reactions which occurred between the ethanol vapor and the samples' sensitive layers when the samples were exposed to gas were also analyzed, and the most probable detection mechanism was deduced. For these measurements, each film

was exposed to six different concentrations of ethanol, namely 100, 200, 300, 400, 500 and 1000 ppm, at its optimum temperature. The duration of each cycle was about 10 min under ethanol vapor. In the overall measurements, dry air was used as a carrier gas.

CTO_{ann} film showed an improvement in ethanol sensitivity compared with the as-prepared sensor CTO_{as} with a switch from n- to p-type conductivity; this result could be attributed to gas interaction with the p-type Co_3O_4 phase formation after the annealing process. In addition, we noted an increase in grain boundaries in the CTO_{ann} sensitive layer which became more granular, with small grains, therefore increasing the density of grain boundaries, which are the favored oxygen adsorption regions. The main reason for the observed grain size decrease is the porosity decrease in the grains with the increase in annealing temperature (i.e., the grain become more compact) as reported in the literature [34]. For working temperatures below 200 °C, the oxygen molecular form O_2^- dominates, and above this temperature the ionic forms O^- and O^{2-} are the predominant adsorbed oxygen species [35]. Thus, the possible ethanol interaction mechanisms with the CTO_{as} film at the optimum temperature of 150 °C could be presented by the following reactions for temperatures below 200 °C:

$$O_{2\ (gas)} + e^-_{(bulk)} \rightarrow O^-_{2(surface)} \quad (6)$$

$$C_2H_5OH_{(gas)} + 3O^-_{2(surface)} \leftrightarrow 3H_2O_{(gas)} + 2CO_{2(gas)} + 3e^-_{(bulk)} \quad (7)$$

The resulting CO_2 and the pre-adsorbed OH^- will react together as follows:

$$CO_{2(gas)} + OH^-_{(surface)} \leftrightarrow HCO^-_{3(surface)} \quad (8)$$

$$HCO^-_{3(surface)} + OH^-_{(surface)} \leftrightarrow CO^{2-}_{3(bulk)} + H_2O_{(gas/surface)} \quad (9)$$

Equation (6) shows that the oxygen molecule is absorbed on the layer's surface without dissociating, by trapping an electron from the bulk, and it becomes negatively charged. After that, the $\left(O_2^-\right)$ adsorbed oxygen species will react with ethanol vapor (C_2H_5OH) to produce water vapor and carbon dioxide (CO_2) and an electron (e^-), according to Equation (7). The carbon dioxide (CO_2) will react with preadsorbed hydroxide (OH^-) according to Equation (8), to provide a reaction product, a bicarbonate ion $\left(HCO_3^-\right)$, which in turn will react with preadsorbed hydroxide OH^- to produce a carbonate anion $\left(CO_3^{2-}\right)$ and water as a final product (Equation (9)).

The resulting negative charges (carbonate anion and electron) will move to the CTO_{as} bulk which, according to the XRD pattern and TEM image already presented in Figures 3 and 4, respectively, present only a pure phase of Co_2SnO_4 and thus increase the carrier charge density. This explains the current increases under ethanol, with the film showing n-type conductivity as already illustrated in Figure 5c at 150 °C. Conversely, for CTO_{ann} film, which presents a phase mixture of Co_2SnO_4/Co_3O_4, we obtained an opposite behavior under ethanol, as also shown in Figure 5c at 200 °C, showing the p-type conductivity which is dominated by the Co_3O_4 species, and which explains the n- to p-type switch observed for annealed film (CTO_{ann}) under ethanol vapor. The probable main ethanol reaction at the optimum temperature of 200 °C for CTO_{ann} is the oxidizing of ethanol given by the following reactions [36]:

$$\frac{1}{2}O_{2(gas)} + e^-_{(bulk)} \rightarrow O^-_{(surface)} \quad (10)$$

$$C_2H_5OH_{(gas)} + O^-_{(surface)} \rightarrow CH_3CHO_{(surface)} + H_2O_{(gas)} + e^-_{(bulk)} \quad (11)$$

Equation (10) shows that the oxygen molecule is absorbed on the layer's surface with dissociation by trapping an electron from the bulk and becoming negatively charged. Following this, the (O^-) adsorbed oxygen species will react with ethanol vapor (C_2H_5OH) to give water vapor, an acetaldehyde molecule (CH_3COH) and an electron (e^-), according to Equation (11).

The electron produced by the previous reaction (Equation (11)) is injected into the bulk, which induces a decrease in the hole concentrations, causing a decrease in current intensity. In this context, Barsan and Weimar show that the preadsorbed ionized form of oxygen in oxide film is produced by the following reaction [35]:

$$\frac{\delta}{2}O_2^{gas} + \alpha\bar{e} + V \rightarrow O_{\delta S}^{-\theta} \quad (12)$$

where V is an oxygen-unoccupied site, $O_{\delta V}^{-\theta}$is the adsorbed oxygen form; $\theta = 1$ for single ionized species, $\delta = 1$ for atomic species. We can infer from this theory that the response S is:

$$S = A[C_{EtOH}]^{\frac{\delta}{\theta+1}} = A[C_{EtOH}]^{\gamma} \text{ where } \gamma = \delta/(\theta+1) \quad (13)$$

The experimental response evolution versus ethanol concentration presented in Figure 5d is in good accordance with Barsan and Weimar's theory. From experimental data, we deduce the fitting of the following γ values:

$\gamma \approx 0.5$ at 200 °C, thus θ = 1 and δ = 1, implying that the layer is porous with small grains

$\gamma \approx 1$ at 150 °C, thus θ = 1 and δ = 2, implying that the layer is compact with large grains

These results confirm our previous proposed mechanisms for ethanol detection by the CTO_{as} and CTO_{ann} layers and are also in good accordance with the morphological investigation reported in Figure 1.

3.2.1. Detection Mechanism under Ethanol

The ethanol response improvement of CTO_{ann} is the result of porosity as well as an increase in grain boundaries. The grain boundary regions are the favored oxygen adsorption regions, as already mentioned above. Consequently, when the proportion of grain boundaries increases in the film due to a decrease in grain size, the oxidation reaction rate became more pronounced for this film wherein the current intensity variation increases due to the increases in charge transfer, and thus the response variation increases. In order to confirm the advanced effects of grains and grain boundaries in the proposed interaction mechanism between ethanol and films, an AC investigation of elaborated films, presented in Figure 6, was performed at the optimum temperatures under 500 ppm of ethanol vapor.

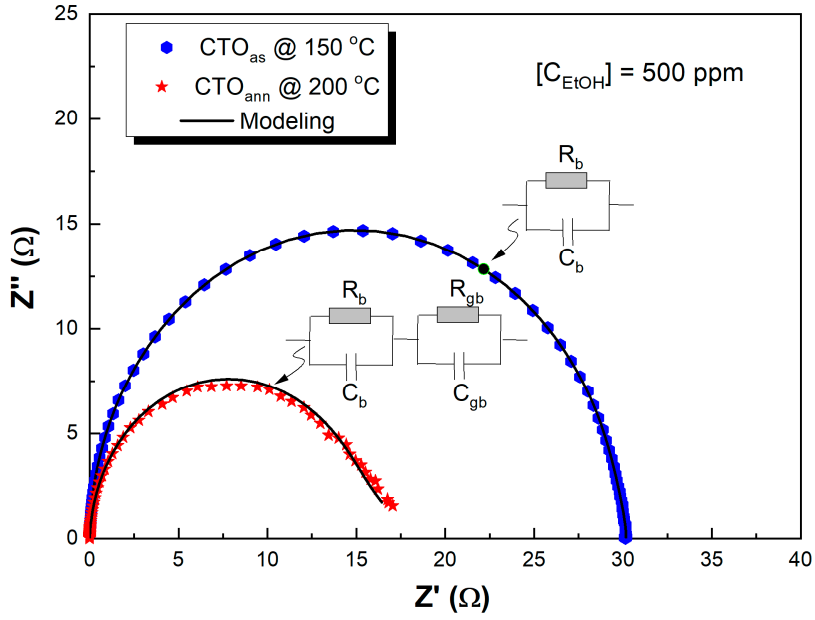

Figure 6. The CTO_{as} and CTO_{ann} AC experimental results and modeling.

The AC analysis evidenced that, under ethanol, the CTO_{as} film impedance could be modelled by a single parallel RC circuit giving one semicircle in a Nyquist plot, attributed to the grain regions. In this case, the CTO_{as} ethanol response is controlled only by the grain regions, whereas for CTO_{ann}, we note the apparition of a second semicircle showing that the response is mainly controlled by the grain boundary regions.

The RC modeling results are reproduced in Table 1, and fit well with the AC experimental results.

Table 1. The RC modeling.

	Film	Under 500 ppm of Ethanol CTO_{as}	Under 500 ppm of Ethanol CTO_{ann}
1St Semicircle	$R_b \times 10^6\ \Omega$	6.44	1257
	$C_b \times 10^{-10}$ F	1.812	1.88
	N	0.996	0.988
2nd Semicircle	$R_{gb} \times 10^6\ \Omega$		79.25
	$C_{gb} \times 10^{-7}$ F		0.391
	N		0.874

The previous results of the AC investigation allow us to affirm that the response enhancement of the CTO_{ann} sensor is mainly controlled by the oxidation reactions with oxygen adsorbed in grain boundary regions formed by Co_3O_4/Co_2SnO_4 p–n heterojunctions. In the other sensor regions there is probably a coexistence of Co_3O_4/Co_3O_4 p–p homojunctions and Co_2SnO_4/Co_2SnO_4 n–n homojunctions, so their electrical (response) behaviors operate against each other.

The CTO_{as} sensor, which presents a pure phase of Co_2SnO_4 according to the XRD pattern and TEM analyses (Figures 3 and 4a), was probably formed only by Co_2SnO_4/Co_2SnO_4 n–n homojunctions. The current variation under ethanol is less than that of the CTO_{ann} sensor formed by Co_3O_4/Co_2SnO_4 p–n heterojunctions. In effect, the mechanism could be related to the contact at the junction interface between Co_3O_4 and Co_2SnO_4 in the heterojunctions and between Co_2SnO_4 and Co_2SnO_4 in the homojunctions, so the sensing property variations for the CTO_{as} and CTO_{ann} semiconductors are controlled by the energy barrier changes "qV" at homojunctions or heterojunctions under ethanol. This energy barrier, in turn, depends on work function differences between Co_3O_4 and Co_2SnO_4 given by the following equation:

$$qV = q(\varnothing_{Co2SnO4} - \varnothing_{Co3O4}) \quad (14)$$

where $\varnothing_{Co3O4}$ and $\varnothing_{Co2SnO4}$ are the work functions for Co_3O_4 and Co_2SnO_4, respectively.

For the Co_2SnO_4/Co_2SnO_4 n–n homojunctions of a pure Co_2SnO_4 layer, the barrier changes will be negligible, whereas for a Co_3O_4/Co_2SnO_4 p–n heterojunction, in the interfaces of the depletion layer the conductivity "G" is mainly determined by the energy barrier changes, presented by the following equation:

$$G \propto Ae^{\left(-\frac{qV}{kT}\right)} \quad (15)$$

where A is a constant, T is the absolute temperature, k is the Boltzmann constant and qV is the effective energy barrier at the interface.

In Figure 7 we have presented the schematic diagram of our proposed sensing mechanism and the energy band structure diagram for the sample CTO_{ann} which contains the

highest density of Co_3O_4/Co_2SnO_4 p–n heterojunctions. This is in order to illustrate the effect of oxygen adsorption on the energy band level and its variations after contact in the grain boundary region before ethanol vapor injection and under ethanol vapor.

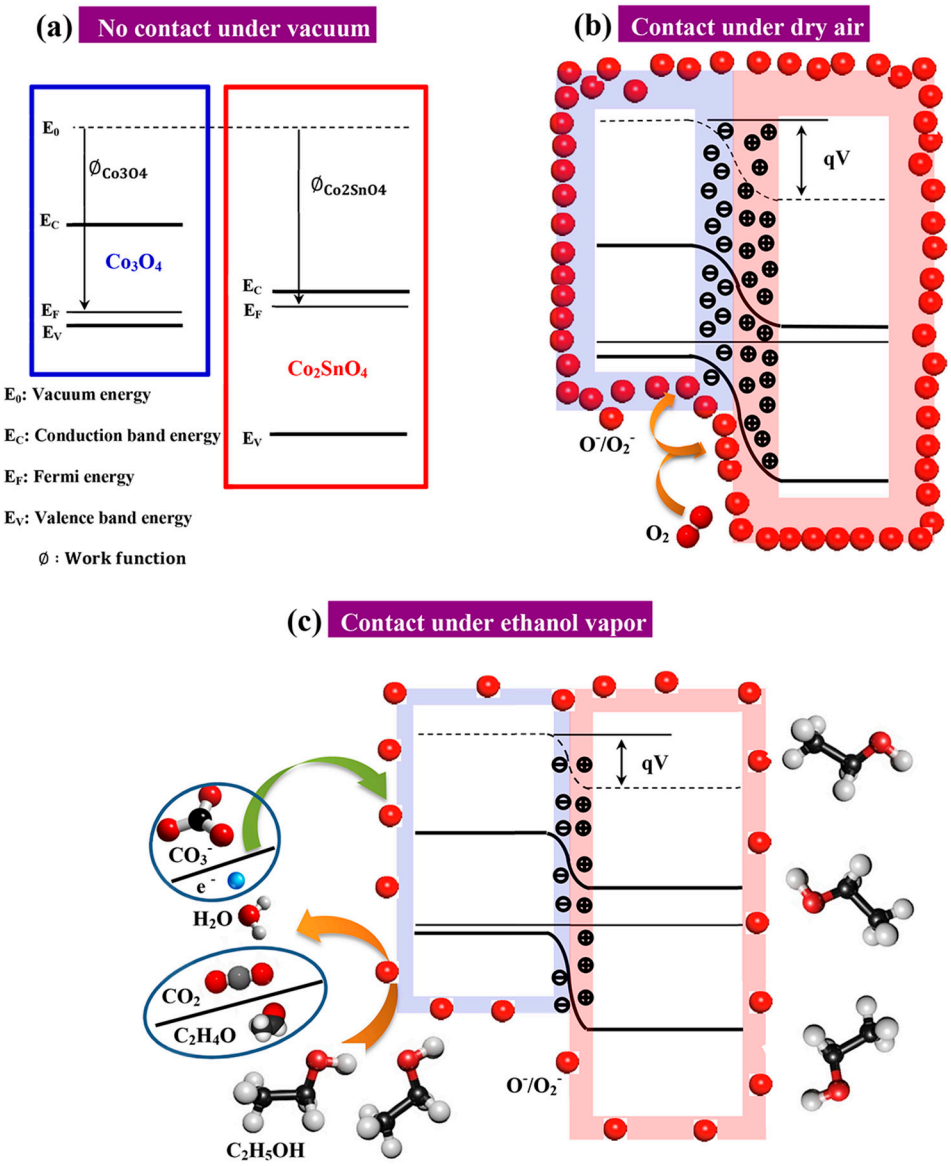

Figure 7. The energy band structure diagram and schematic diagram of the sensing mechanism of Co_3O_4/Co_2SnO_4 p–n heterojunctions (CTO_{ann}): (**a**) no contact under vacuum; (**b**) contact under dry air and (**c**) contact under ethanol vapor.

Figure 7b schematizes the oxygen adsorption reactions given by Equations (6) and (10) when the sample is under a fixed flow of dry air before ethanol injections, and Figure 7c schematizes the possible oxidation reactions given by Equations (7) and (11) from the interactions between ethanol and adsorbed oxygen on the surface of the layer in the grain boundaries.

3.2.2. Response Stability under Ethanol

After mechanism deduction, an investigation of the annealing process effect on the response stability under ethanol was also conducted. Figure 8 presents the response stability of each sample under an ethanol vapor concentration of 500 ppm at the optimum temperature, for a duration of three months. As presented in Figure 7a, we note that for CTO_{as} the stability deteriorated after the first month, and the layer response drift increased

to reach 35% at the third month, whereas CTO_{ann} response drift did not exceed 5%. The result shows an improvement in stability following the annealing process, as well as sensibility toward ethanol vapor. In addition, in our previous work [37] we demonstrated that humidity has a neglected effect on the response stability of Co_2SnO_4. Thus, we think that the Co_2SnO_4/Co_3O_4 composite which presented better stability will be not affected by humidity; this prediction could be investigated in future research. Moreover, a comparative study of CTO_{ann} sensing parameters with those of other sensing materials under the concentration range 500–600 ppm of ethanol vapor, which is situated in our concentration range, are presented in Table 2. These further reveal the good performance of our Co_2SnO_4/Co_3O_4 composite (CTO_{ann}).

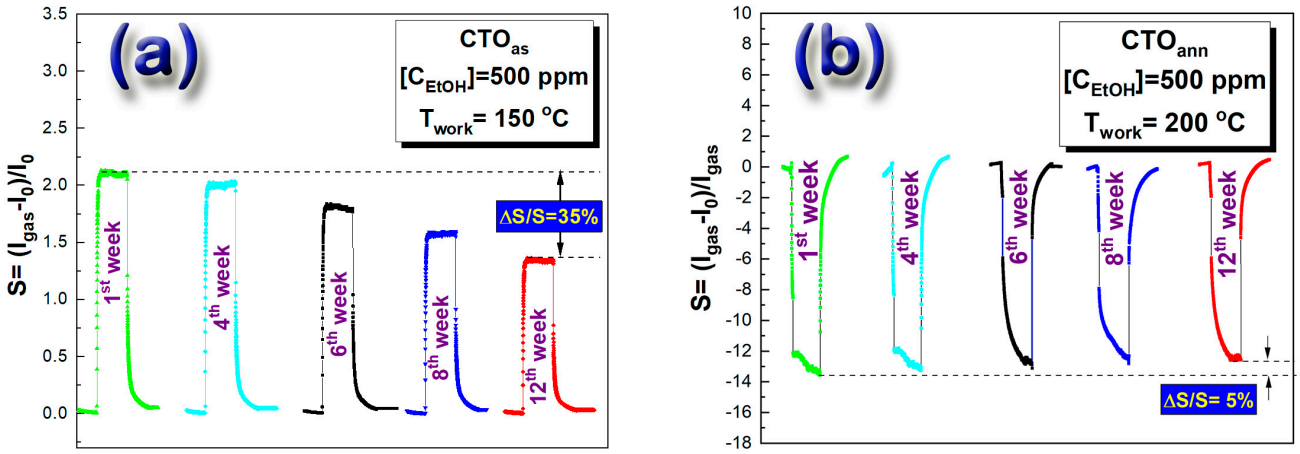

Figure 8. Stability investigation of samples under 500 ppm of ethanol vapor at the optimum temperatures: (**a**) CTO_{as} and (**b**) CTO_{ann}.

Table 2. Comparative study of Co_2SnO_4/Co_3O_4 composite (CTO_{ann}) ethanol sensing parameters with other ethanol sensing materials.

Sensor Material	Fabrication Approach	Conc. (ppm)	Response "S"	Sens Temp. (°C)	τ_{res}/τ_{rec} (s)	Ref.
Co_2SnO_4 spinel thin film	Spray pyrolysis	500	3.5	150	20/24	[37]
SnO_2 (triton)	Spin coating	500	3	RT	15/720	[38]
Zn_2SnO_4 spinel cube	Hydrothermal	600	5.5	325	18/45	[39]
α-Fe_2O_3 nanorods	Hydrothermal	500	8	220	−/−	[40]
Porous SiC	Electrochemical etching	Saturated vapors	1.2	RT	85/57	[41]
$NiCo_2O_4$ spinel nanoparticles	Hydrothermal	500	0.6	RT	20/26	[42]
TiO_2 NWs	Electrospinning	500	7.5	500	23/1	[43]
Cu_2O nano-columnar	GLAD technique	500	8.12	200	60/180	[44]
Zn_2SnO_4cuboctahedra	Chemical method	600	0.01	325	18/45	[45]
Co_2SnO_4/Co_3O_4 composite	Spray pyrolysis	500	13.5	200	35/30	This work

4. Conclusions

In conclusion, the annealing process of Co_2SnO_4 film synthesized by spray pyrolysis method, denoted as CTO_{as}, is beneficial for ethanol detection. After annealing, we successfully obtained the Co_2SnO_4/Co_3O_4 composite, denoted as CTO_{ann}. The new composite presents an improvement in response under ethanol at the optimal temperature of 200 °C, due to the increases in its porosity and grain boundary density, which offers a more specific

surface for oxygen adsorption. Further, we observed an improvement in the film's stability compared with the non-annealed one. We also noted that after the annealing process the Co_2SnO_4 film underwent a switching from n- to p-type conductivity under ethanol, due to the p-type Co_3O_4 phase formation in the Co_2SnO_4 structure. The sensing mechanism was found to be an oxidation reaction which depends on the working temperature, resulting in negative charges, such as a carbonate anion for CTO_{as} because the oxidation reaction of ethanol occurs with O^{2-} at the optimal temperature of 150 °C, and an electron for CTO_{ann} because the oxidation reaction of ethanol occurs with O^{-}. at the optimal temperature of 200 °C. The resulting charges will be moved to the bulk of the samples, which raises the current intensity due to the increase in the electron density in the CTO_{as} layer (n-type conductivity) and decreases the current intensity for CTO_{ann} due to the decrease in hole density after recombination with electrons (n-type conductivity). The improvement in responses was explained by the increase in grain boundary heterojunctions in the CTO_{ann} film, wherein the conductivity was controlled by the energy barrier changes.

Finally, the stability of CTO_{as} and CTO_{ann} over a period of three months was investigated; the results show an improvement in stability after the annealing process.

In future work, we intend to investigate the effects of layer thicknesses and electrode architecture on the sensor responses and selectivity. The primary results of our investigation into the effect of the annealing process on the film's sensing properties under ethanol vapor presented in the present work show that CTO_{ann} is promising for application as a sensitive active layer for ethanol sensor devices in the future.

Funding: This study was funded by the Deputyship for Research & Innovation, Ministry of Education, Saudi Arabia, through project number QU-IF-4-5-1-29587.

Data Availability Statement: The data presented in this study are available on request from the corresponding author. The data are not publicly available because some data are proprietary or confidential. Therefore, the data may only be provided with restrictions (e.g., anonymized data).

Acknowledgments: The authors extend their appreciation to the Deputyship for Research& Innovation, Ministry of Education, Saudi Arabia for funding this research work through the project number (QU-IF-4-5-1-29587). The authors also thank to Qassim University for technical support.

Conflicts of Interest: The author declares no conflict of interest.

References

1. Kaneti, Y.V.; Moriceau, J.; Liu, M.; Yuan, Y.; Quadir, M.Z.; Jiang, X.; Yu, A. Hydrothermal synthesis of ternary α-Fe_2O_3–ZnO–Au nanocomposites with high gas-sensing performance. *Sens. Actuators B Chem.* **2015**, *209*, 889–897. [CrossRef]
2. Gawli, Y.; Badadhe, S.; Basu, A.; Guin, D.; Shelke, M.V.; Ogale, S. Evaluation of n-type ternary metal oxide $NiMn_2O_4$ nanomaterial for humidity sensing. *Sens. Actuators B Chem.* **2014**, *191*, 837–843. [CrossRef]
3. Mohanta, D.; Ahmaruzzaman, M. Novel Ag-SnO_2-βC_3N_4 ternary nanocomposite based gas sensor for enhanced low-concentration NO_2 sensing at room temperature. *Sens. Actuators B Chem.* **2021**, *326*, 128910. [CrossRef]
4. Pfaff, G. Wet chemical synthesis of $BaSnO_3$ and Ba_2SnO_4 powders. *J. Eur. Ceram. Soc.* **1993**, *35*, 3017–3021. [CrossRef]
5. Ishigaki, T.; Torisaka, A.; Nomizu, K.; Madhusudan, P.; Uematsu, K.; Toda, K.; Sato, M. Long phosphorescent Ca_2SnO_4 with minuscule rare earth dopant concentration. *Dalton Trans.* **2013**, *42*, 4781–4785. [CrossRef]
6. Wang, W.; Xiao, Y.; Zhao, X.; Liu, B.; Cao, M. Synthesis of Cd_2SnO_4–SnO_2 hybrid micro-cubes with enhanced electrochemical performance for lithium-ion batteries. *CrystEngComm* **2014**, *16*, 922–929. [CrossRef]
7. Lei, S.; Tang, K.; Chen, C.; Jin, Y.; Zhou, L. Preparation of Mn_2SnO_4 nanoparticles as the anode material for lithium secondary battery. *Mater. Res. Bull.* **2009**, *44*, 393–397. [CrossRef]
8. Al-Shahrani, A.A. Sintering behavior and thermal property of Mg_2SnO_4. *J. Mater. Sci.: Mater. Electron.* **2005**, *16*, 193–196. [CrossRef]
9. Zhao, Y.; Li, X.; Yan, B.; Xiong, D.; Li, D.; Lawes, S.; Sun, X. Recent Developments and Understanding of Novel Mixed Transition-Metal Oxides as Anodes in Lithium Ion Batteries. *Adv. Energy Mater.* **2016**, *6*, 1502175. [CrossRef]
10. Aguilar-Martinez, J.; Pech-Canul, M.; Esneider, M.; Toxqui, A.; Shaji, S. Synthesis, structure parameter and reaction pathway for spinel-type Co_2SnO_4. *Mater. Lett.* **2012**, *78*, 28–31. [CrossRef]
11. Chen, C.; Ru, Q.; Hu, S.; An, B.; Song, X.; Hou, X. Co_2SnO_4 nanocrystals anchored on graphene sheets as high-performance electrodes for lithium-ion batteries. *Electrochim. Acta* **2015**, *151*, 203–213. [CrossRef]

12. Thota, S.; Narang, V.; Nayak, S.; Sambasivam, S.; Choi, B.; Sarkar, T.; Andersson, M.; Mathieu, R.; Seehra, M. On the nature of magnetic state in the spinel Co_2SnO_4. *J. Phys. Condens. Matter.* **2015**, *27*, 166001. [CrossRef]
13. Qi, Y.; Du, N.; Zhang, H.; Wu, P.; Yang, D. Synthesis of Co_2SnO_4@C core–shell nanostructures with reversible lithium storage. *J. Power Sources* **2011**, *196*, 10234–10239. [CrossRef]
14. Dinesh, S.; Barathan, S.; Premkumar, V.K.; Sivakumar, G.; Anandan, N. Hydrothermal synthesis of zinc stannate (Zn_2SnO_4) nanoparticles and its application towards photocatalytic and antibacterial activity. *J. Mater. Sci.: Mater. Electron.* **2016**, *27*, 9668–9675. [CrossRef]
15. Alpuche-Aviles, M.; Wu, Y. Photoelectrochemical Study of the Band Structure of Zn_2SnO_4 Prepared by the Hydrothermal Method. *J. Am. Chem. Soc.* **2009**, *131*, 3216–3224. [CrossRef]
16. Oh, L.; Kim, D.; Lee, J.; Shin, S.; Lee, J.; Park, I.; Ko, M.; Park, N.; Pyo, S.; Hong, K.; et al. Zn_2SnO_4-Based Photoelectrodes for Organolead Halide Perovskite Solar Cells. *J. Phys. Chem. C* **2014**, *118*, 22991–22994. [CrossRef]
17. Chen, Z.; Cao, M.; Hu, C. Novel Zn_2SnO_4 Hierarchical Nanostructures and Their Gas Sensing Properties toward Ethanol. *J. Phys. Chem. C* **2011**, *115*, 5522–5529. [CrossRef]
18. He, P.; Xie, Z.; Chen, Y.; Dong, F.; Liu, H. Co_2SnO_4/activated carbon composite electrode for supercapacitor. *Mater. Chem. Phys.* **2012**, *137*, 576–579. [CrossRef]
19. Balasubramaniam, G.S.R.; Bhuvaneshwari, S.; Wu, J.J.; Abdullah, M.A.; Sambandam, A. Sonochemical synthesis of Co_2SnO_4 nanocubes for super capacitor applications. *Ultrason Sonochem.* **2018**, *41*, 435–440.
20. Choi, K.I.; Kim, H.R.; Kim, K.M.; Liu, D.; Gao, G.; Lee, J.H. C_2H_5OH sensing characteristics of various Co_3O_4 nanostructures prepared by solvothermal reaction. *Sens. Actuators B Chem.* **2010**, *146*, 183–189. [CrossRef]
21. Sun, C.; Su, X.; Xiao, F.; Niu, C.; Wang, J. Synthesis of nearly monodisperse Co_3O_4 nanocubes via a microwave-assisted solvothermal process and their gas sensing properties. *Sens. Actuators B Chem.* **2011**, *157*, 681–685. [CrossRef]
22. Wen, Z.; Zhu, L.; Mei, W.; Hu, L.; Li, Y.; Sun, L.; Cai, H. Rhombus-shaped Co_3O_4 nanorod arrays for high-performance gas sensor. *Sens. Actuators B Chem.* **2013**, *186*, 172–179. [CrossRef]
23. Li, B.; Liu, J.; Liu, Q.; Chen, R.; Zhang, H.; Yu, J.; Song, D. Core-shell structure of ZnO/Co_3O_4 composites derived from bimetallic organic frameworks with superior sensing performance for ethanol gas. *Appl. Surf. Sci.* **2019**, *475*, 700–709. [CrossRef]
24. Chen, X.; Liang, R.; Qin, C.; Ye, Z.; Zhu, L. Coaxial electrospinning Fe_2O_3@Co_3O_4 double-shelled nanotubes for enhanced ethanol sensing performance in a wide humidity range. *J. Alloys Compd.* **2022**, *891*, 161868. [CrossRef]
25. Li, G.; Zhang, Y.; Liang, Q.; Zhang, J.; Liu, J. Nanoporous Co_3O_4–TiO_2 Heterojunction Nanosheets for Ethanol Sensing. *ACS Appl. Nano Mater* **2022**, *5*, 4779–4786. [CrossRef]
26. Bu, X.; Ma, F.; Wu, Q.; Wu, H.; Yuan, Y.; Hu, L.; Han, C. Metal-organic frameworks-derived Co_3O_4/$Ti_3C_2T_x$ Mxene nanocomposites for high performance ethanol sensing. *Sens. Actuators B Chem.* **2022**, *369*, 132232. [CrossRef]
27. Mhamdi, A.; Labidi, A.; Souissi, B.; Kahlaoui, M.; Yumak, A.; Boubaker, K.; Amlouk, A.; Amlouk, M. Impedance spectroscopy and sensors under ethanol vapors application of sprayed vanadium-doped ZnO compounds. *J. Alloys Compd.* **2015**, *639*, 648–658. [CrossRef]
28. Umar, A.; Al-Hazmi, F.; Dar, G.N.; Zaidi, S.A.; Al-Tuwirqi, R.M.; Alnowaiserb, F.; Al-Ghamdi, A.A.; Hwang, S. Ultra-sensitive ethanol sensor based on rapidly synthesized $Mg(OH)_2$ hexagonal nanodisks. *Sens. Actuators B Chem.* **2012**, *166*, 97–102. [CrossRef]
29. Tiemann, M. Porous Metal Oxides as Gas Sensors. *Chem. Eur. J.* **2007**, *13*, 8376–8388. [CrossRef]
30. Chakraborty, G.; Pugazhenthi, G.; Katiyar, V. Exfoliated graphene-dispersed poly (lactic acid)-based nanocomposite sensors for ethanol detection. *Polym. Bull.* **2019**, *76*, 2367–2386. [CrossRef]
31. Labidi, A.; Gillet, E.; Delamare, R.; Maaref, M.; Aguir, K. Ethanol and ozone sensing characteristics of WO_3 based sensors activated by Au and Pd. *Sens. Actuators B Chem.* **2006**, *120*, 338–345. [CrossRef]
32. Labidi, A.; Bejaoui, A.; Ouali, H.; Chaffar Akkari, F.; Hajjaji, A.; Gaidi, M.; Kanzari, M.; Bessaïs, B.; Maaref, M. Dry air effects on the copper oxides sensitive layers formation for ethanol vapor detection. *Appl. Surf. Sci* **2011**, *257*, 9941–9945. [CrossRef]
33. Muzny, C.D.; Diky, V.; Kazakov, A.; Chirico, R.D.; Frenkel, M. Vapor Pressure. In *CRC Handbook of Chemistry and Physics*, 95th ed.; Haynes, W.M., Ed.; CRC Press Taylor and Francis Group: Boca Raton, FL, USA; New York, NY, USA; Philadelphia, PA, USA, 2014; Volume 6, pp. 6–96.
34. Khalifa, Z.S. Grain size reduction on nanostructured TiO_2 thin films due to annealing. *RSC Adv.* **2017**, *7*, 30295–30302. [CrossRef]
35. Barsan, N.; Weimar, U. Conduction model of metal oxide gas sensors. *J. Electroceram.* **2001**, *7*, 143–167. [CrossRef]
36. Hellegouarc'h, F.; Arefi-Khonsari, F.; Planade, R.; Amouroux, J. PECVD prepared SnO_2 thin films for ethanol sensors. *Sens. Actuators B Chem.* **2001**, *73*, 27–34. [CrossRef]
37. Labidi, A. Novel ethanol sensing properties of sprayed ternary Co_2SnO_4 thin layer. *Mater. Lett.* **2021**, *294*, 129784. [CrossRef]
38. Belaqziz, M.; Amjoud, M.; Gaddari, A.; Rhouta, B.; Mezzane, D. Enhanced room temperature ozone response of SnO_2 thin film sensor. *Superlattices Microstruct.* **2014**, *71*, 185–189. [CrossRef]
39. Jiang, Y.Q.; Chen, X.X.; Sun, R.; Xiong, Z.; Zheng, L.S. Hydrothermal syntheses and gas sensing properties of cubic and quasi-cubic Zn_2SnO_4. *Mater. Chem. Phys.* **2011**, *129*, 53–61. [CrossRef]
40. Robbie, K.; Sit, J.C.; Brett, M.J. Advanced techniques for glancing angle deposition. *J. Vac. Sci. Technol. B* **1998**, *16*, 1115–1122. [CrossRef]
41. Tait, R.N.; Smy, T.; Brett, M.J. Modelling and characterization of columnar growth in evaporated films. *Thin Solid Films* **1993**, *226*, 196–201. [CrossRef]

42. Balaji, G.; Rathinavel, S.; Vadivel, S. Design and fabrication of clad removed fiber optic based $NiCo_2O_4$ sensor for detection of ethanol and acetone gases. *Optik* **2021**, *228*, 166216. [CrossRef]
43. Dirks, A.G.; Leamy, H.J. Columnar microstructure in vapor-deposited thin films. *Thin Solid Films* **1977**, *47*, 219–233. [CrossRef]
44. Ben Nacer, S.; Jlidi, D.; Labidi, A.; Chaffar Akkari, F.; Touihri, S.; Maaref, M. Promising ethanol detection enhancement of Cu_2O thin film deposited by GLAD technique. *Measurement* **2020**, *151*, 107208. [CrossRef]
45. Zhu, C.L.; Chen, Y.J.; Wang, R.X.; Wang, L.J.; Cao, M.S.; Shi, X.L. Synthesis and enhanced ethanol sensing properties of α-Fe_2O_3/ZnO hetero nanostructures. *Sens. Actuators B Chem.* **2009**, *140*, 185–189. [CrossRef]